Spectral Energy Model-Driven Inversion of XCO$_2$ in IPDA Lidar Remote Sensing

Haowei Zhang, Ge Han, Xin Ma, Siwei Li, Hao Xu, Tianqi Shi, Jianye Yuan, Wanqin Zhong, Yanran Peng, Jingjing Xu, and Wei Gong, *Member, IEEE*

Abstract— Carbon observation satellites based on passive theory (e.g., OCO-2/3, GOSAT-1/2, and TanSat) have relatively high carbon dioxide column concentration (XCO$_2$) accuracy when the observation conditions are met. Passive satellites have data bias and coverage deficiencies due to cloud cover, low albedo, low-light conditions, and aerosol scattering, resulting in carbon observation satellites based on passive theory that cannot meet the demand for high-precision, all-day, all-weather XCO$_2$ monitoring. Active detection satellites are urgently needed to support global carbon sources, sinks, and carbon neutrality. China intends to launch a sensor satellite with active detection of XCO$_2$ in the coming years. In this work, based on the satellite's scaled-down airborne experiments, a spectral energy model was developed to optimize the conventional inversion algorithm and achieve a more accurate XCO$_2$ inversion. The 1.572-μm integrated path differential absorption (IPDA) lidar column length is used indirectly to evaluate the accuracy of the spectral energy model for signal extraction. Also, the experimental results show that the accuracy of the signal extracted by the 1.572-μm IPDA lidar column length is 0.74 and 6.20 m at sea and on land based on the indirect evaluation of the length of the 1.572-μm IPDA lidar column length. The optimized XCO$_2$ was evaluated (standard deviation as an evaluation metric) and its XCO$_2$ standard deviation reduced by 31%, 63%, and 66% in the ocean, plains, and mountains, respectively. Our algorithm can obtain the XCO$_2$ with a consistent trend by using XCO$_2$ from the OCO-2 satellite as a reference. The calculated XCO$_2$ is more accurate in areas dominated by anthropogenic factors (plains), due to the accuracy of the IPDA detection mechanism. This algorithm improves the accuracy and robustness of XCO$_2$ inversion and has important reference significance for the IPDA lidar carried by China's satellites to be launched in this year.

Haowei Zhang, Jianye Yuan, Yanran Peng, Jingjing Xu, and Wei Gong are with the School of Electronic Information, Wuhan University, Wuhan 473072, China (e-mail: haoweizhang@whu.edu.cn; yuan666@whu.edu.cn; 2021282120109@whu.edu.cn; xu_jingjing@whu.edu.cn; weigong@whu.edu.cn).

Ge Han and Siwei Li are with the School of Remote Sensing and Information Engineering, Wuhan University, Wuhan 430079, China (e-mail: udhan@whu.edu.cn; siwei.li@whu.edu.cn).

Xin Ma, Hao Xu, Tianqi Shi, and Wanqin Zhong are with the State Key Laboratory of Information Engineering in Surveying, Mapping, and Remote Sensing, Wuhan University, Wuhan 430079, China (e-mail: maxinwhu@whu.edu.cn; xiaohao190081@whu.edu.cn; shitian@whu.edu.cn; 2021206190052@whu.edu.cn).

Digital Object Identifier 10.1109/TGRS.2023.3238117

Index Terms— Active monitoring, integrated path differential absorption (IPDA), XCO$_2$.

I. INTRODUCTION

THE greenhouse effect, caused by the rapid increase in anthropogenic emissions of primary greenhouse gases (CO$_2$, CH$_4$, and N$_2$O) around the world, is affecting the ecosystem health and economic advancement. Since the industrial revolution in the last century, the global CO$_2$ gas concentration has increased from 278 ppm (prior to the industrialization era) to 410 ppm in 2020 [1]. However, the global CO$_2$ concentration increase of 10 ppm took five years from 2015 to 2020 [2]. Despite the government's lockdown measures during the epidemic, the growth rate of the CO$_2$ column concentration (XCO$_2$) was slowed down by 0.08–0.23 ppm/year relative to the growth rate of 2 ppm/year. In addition, as we approach the goal of reaching the carbon peak in 2030 in China [3], an efficient carbon monitoring technology must be developed to accurately quantify the sources and sinks of CO$_2$. Currently, the theory of XCO$_2$ monitoring is mainly divided into passive and active. Passive monitoring relies on measuring the reflected sunlight spectrum in the infrared region over the globe to retrieve the column-averaged XCO$_2$ (e.g., GOSAT, GOSAT-2, OCO-2, OCO-3, and TanSat missions). The principle of active XCO$_2$ detection is the integrated path differential absorption (IPDA) [4], [5], [6], [7], [8], [9], [10], which measures the differential absorption of CO$_2$ by using two laser beams as light sources, followed by retrievals to determine the XCO$_2$ along the laser light path.

This capability is insufficient to achieve for the passive spectrometers using reflected sunlight due to aerosol scattering, low coverage at high latitudes, and the inability to observe throughout the day [11], [12], [13], [14], [15], [16], [17], [18], [19]. We need to combine active and passive XCO$_2$ detection equipment to accurately quantify the sources and sinks of CO$_2$. Currently, many scholars have carried out some studies on XCO$_2$ based on IPDA lidar. Abshire et al. [20] conducted the 1.572-μm IPDA lidar ASCENDS science flight experiment in 2011, obtaining a 2–3-ppm error in a relatively constant XCO$_2$ area based on 10-s data averaging. Refaat et al. [21] carried out 2.0-μm IPDA lidar experiments in 2014 and performed modeling based on the obtained profiles over the sea and land, and their results reduced the range bias of the CO$_2$ pulses. Singh et al. [22] conducted a simulation experiment in 2017 that resulted in an expected performance of less than 0.35 ppm based on 10-s data averaging. Zhu et al. [23] carried out 1.572-μm IPDA lidar experiments in China and confirmed the validity of the airborne experiments by evaluating the

Fig. 1. Map of the flight track over the Qinhuangdao in China on March 14, 2019.

TABLE I
PARAMETERS OF THE USED 1.572-μM IPDA LIDAR

Parameter Name	Value	Parameter Name	Value
Platform height/km	around 6.9	Pulse width/ns	15–20
Lidar energy/mJ	6	Lidar pulse repetition rate/Hz	20
On-line wavelength/nm	1572.024	Lidar divergence angle/mrad	0.62
Off-line wavelength/nm	1572.085	Field angle of the receiver/mrad	1.0
Repetition frequency/Hz	20 (double pulse)	Telescope diameter/m	0.15
Sampling rate/MHz	125	Beam emission interval/us	200

whole detection system hardware. Xiang et al. [24] carried out a program design for XCO_2 inversion based on the 1.572-μm IPDA flight experiment in China. The results showed that the predicted relative random error of XCO_2 was less than 0.3% for the forthcoming satellite mission over land.

Although many of the abovementioned scholars have carried out the inversion of XCO_2 based on the IPDA lidar, the hardware equipment is different in different teams. Therefore, the format of the IPDA echo signal and the algorithm to optimize or invert the XCO_2 data (mostly based on idealized Gaussians) are also different. Besides, considering that the obtained data are non-Gaussian shaped from our team, thus, this article proposes an algorithmic framework to reduce the errors caused by the non-Gaussian data and the differential absorption optical thickness (DAOD) and integral weight function (IWF) separation calculations during the airborne signal processing. Therefore, we propose a model based on spectral energy that can match non-Gaussian signal waveforms from the experiments, especially for multiple subwaveform echoes from mountains or clouds. It can also be used to obtain the optimized XCO_2 based on the simultaneously optimized DAOD and IWF from the parameter set information combined with (1). Also, the core principle of this spectral energy model is to construct the spectral energy model in advance and extract the parameters of the multiwaveform signal based on the above equations [in (2)]. Then, the fit parameters are optimized based on the Levenberg–Marquardt (LM) algorithm with the spectral energy model as the core. The optimization of the IWF is achieved by direct leveling with unequal accuracy. Finally, we reduce the signal energy by definite integration using the optimized parameters to improve the DAOD. This inversion method takes the spectral energy model as the core and focuses on the parameter transfer and optimization to improve the calculation accuracy of the IWF and the optical differential absorption thickness. Therefore, this theory can effectively optimize the traditional XCO_2 algorithm and further improve the accuracy of IPDA lidar detection to support the analysis of carbon sources and sinks.

The remaining parts of this work are arranged as follows. The data and method we used are described in Section II. The main results and discussions are demonstrated in Section III. Finally, we conclude the whole study in Section IV.

II. DATA

In March 2019, aircraft equipped with IPDA lidar was used to detect the CO_2 column concentration along a predetermined route. In this work, we selected the portion of the flight data during the experiment for algorithm verification, and the altitudes of the selected data were mainly concentrated at 7 km. We also present the experiment path and the terrain slope in Fig. 1 to clearly show the flight trajectory. The overall flight trajectory of the aircraft mainly covered the sea area around Qinhuangdao in China (see Fig. 1).

The experimental data obtained in the research area comprise 13 files, in which a single file contains 4000 data packets. Each packet contains an observation pair and 22 000 float data, namely, ON and OFF wavelength pulse-echo signals, corresponding to 11 000 float data. The first 11 data of each observation pair also contain the current aircraft attitude information, global positioning system (GPS) cycle second information, longitude and latitude, altitude, course speed, and other information. Some of the equipment's information is shown in Table I.

The ICESat-2_ATL08_V4 product is used to obtain the elevation values of the ground in the Qinhuangdao area from December 2018 to December 2021 to further verify the optimized integral weighting function results. Then, the elevation values are used as the input parameters for comparison verification. The ICESat-2 and experimental data are based on the WGS84 coordinate system. The WGS84 coordinate system is a geocentric coordinate system that contains a set of standard latitude and longitude coordinate systems of the Earth and it is a reference ellipsoid used to calculate raw elevation data. Some scholars have verified the ICESat-2 data, and the mean of height error of ICESat-2_ATL08 terrain is less than 0.05 m in the plain region and 0.5 m in the mountain region [25]. Therefore, we validated the model using ICESat-2_ATL08 data at the ground surface.

III. THEORETICAL FRAMEWORK

The proposed algorithmic framework focuses on two main aspects in this work to obtain a high-precision XCO_2. First, we incorporate (1) to optimize the accuracy of the laser column length and obtain the optimization of the IWF from the denominator's perspective. Second, this work incorporates
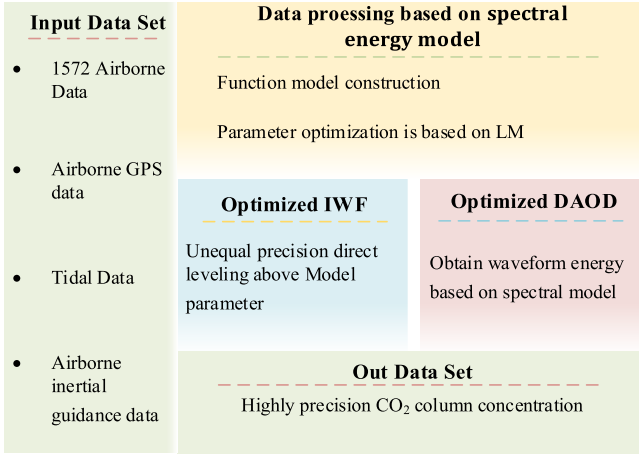
Fig. 2. Framework of the proposed methodology.

(1) to optimize the energy integral of the waveform to obtain the DAOD from the numerator's perspective. Fig. 2 shows the algorithm framework flowchart

$$XCO_2 = \frac{DAOD}{IWF} = \frac{\frac{1}{2} \times \ln\left(\frac{P_{OFF}}{E_{OFF}} / \frac{P_{ON}}{E_{ON}}\right)}{\int_{P_0}^{P_{SFC}} WF_{CO2}(p)d_p} \quad (1)$$

where XCO_2 is the CO_2 concentration after inversion; DAOD is the differential absorption optical thickness; IWF is the integral weight function; P and E are the ground echo and output energies, respectively, which are measured at a corresponding online or offline wavelength; $WF_{CO_2}(p)$ is the weighted function of CO_2; and P_{SFC} and P_0 are the integral upper and lower limit parameters determined by ranging information, meteorological parameters, and aircraft inertial guidance information, respectively.

A. Function Model Construction

The echo signal of lidar is regarded as the superposition of several Gaussian signals, and it has the characteristics of approximate symmetry. However, this characteristic is affected by terrain and causes signal broadening. The broadened signal is difficult to quantitatively describe by using a single equation, which increases the calculation error of DAOD and IWF. We propose a new theory [see (2)] for waveform modeling based on the spectral energy model for the 1.572-μm IPDA lidar echo signal, which can reduce the calculation errors of DAOD and IWF caused by broadened signal because the conventional waveform fitting cannot be accurately described by the Gaussian model [26]. We combine multiple parameters based on (2) with the real signal situation of 1.572-μm IPDA lidar echo signal in the experiment to ensure that the influence of the modified model can reduce the broadening effect of waveform. Moreover, the characteristic parameters of the signal are obtained through the quantitative expression of the whole echo signal formula. The spectral energy formula and the modified formula are given as follows:

$$F(x) = h - c \cdot \frac{e^{g(x-d)\left(\frac{1}{a} - \frac{1}{b}\right)}}{e^{g(x-d)\left(\frac{1}{a} + \frac{1}{b}\right)} + e^{-g(x-d)\left(\frac{1}{a} + \frac{1}{b}\right)}} \quad (2)$$

where $a = 1/4(1/\tau_r - 1/\tau_f)$ and $b = 1/4(1/\tau_r + 1/\tau_f)$, and τ_r and τ_f are the rise and fall times, respectively. In (2),

parameter d is the center of the waveform component and represents the distance of the signal transmission. Also, the parameter g is a constant. The remaining parameters (a, b, c, and h) reduce the waveform equation from the discrete data. Parameters a, b, c, d, and h must be obtained by fitting.

We adopted the LM algorithm based on (2) as the core to obtain accurate model parameters for the echo signals of multiple land use types. The LM algorithm can be deeply optimized based on the previous model parameters, combined with the corresponding constraints, to obtain nonlinear fitting results that meet the accuracy requirements.

B. Optimized IWF and DAOD From the Above Model

During the optimization of the IWF, we mainly focus on the modification of the upper and lower limits in IWF. When the CO_2 column length error is less than 3 m, the experimental results show that the error of the XCO_2 column using the IPDA lidar system in space is less than 1%. Improving the IWF inversion is feasible from the perspective of the accurate measurement of the CO_2 column length by combining the optimized parameter d of the above model.

The IPDA lidar transmitter emits 1.57-μm online and offline beams in parallel at a 200-μs interval. Accordingly, this transmitter can be regarded as two consecutive distance measurements of the same target, thereby generating redundant observations of the ranging information. Although the LM algorithm is based on (2), the distance measurement observation value still has an error relative to the true value. Given that the distances were separately measured for the online and offline bands, the distance measurement values generated by the two observations should be slightly different. To balance this difference, we introduce the direct adjustment theory of unequal precision. In terms of the measurement adjustment, we generally consider weight as the relative evaluation index of the reliability of observation results, which is inversely proportional to the square of the median error. The most probable value formula is used to obtain the high-precision range values. The weight and the most probable value formula are given as follows:

$$L = c_{light} * d_{Op}/(2f) \quad (3)$$

$$P_n = \frac{1}{m_n^2} \quad (4)$$

$$x = \frac{\sum_{n=1}^{2} P_n \times L}{\sum_{n=1}^{2} P_n} \quad (5)$$

where L is the measurement value of the online or offline bands processed from the above data; c_{light} is the speed of light; d is the center of the waveform component and represents the distance of the signal transmission; f is the 1.572-μm IPDA lidar sampling frequency; m_n^2 is the median error corresponding to the online or offline bands, and this median error refers to the standard deviation of 100 counts before the start of the valid signal; P_n is the weight corresponding to the online or offline bands; and x is the optimized high-precision ranging value.

During the optimization of the DAOD, we mainly fit the signal waveform based on the proposed model equation to
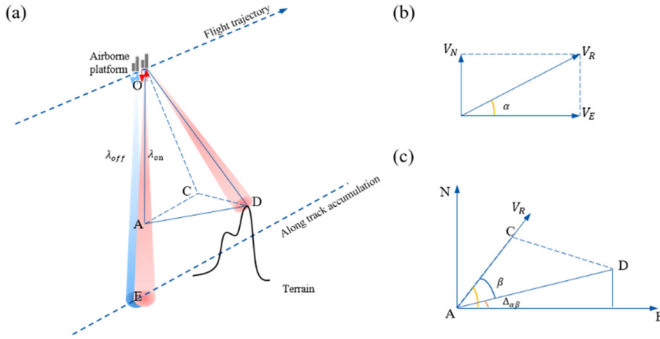
Fig. 3. Geographic model of the lidar footprints deviating from the sub-aircraft points. Point O represents the location where the 1.572-μm IPDA lidar signal is emitted. Point D represents the reflection position of the 1.572-μm IPDA lidar signal when it touches the ground. Point A is a point on the sub-aircraft path (OA), and its height is on the same plane as point D. Points C, A, and B are in the same elevation plane, and the angles formed by points A, O, and C are equal to the pitch angle. In (c), this N and E represent the north and east in the coordinate axes, respectively.

obtain an accurate description of the signal equation. Furthermore, we integrate the equation to restore the energy of the signal according to the restored model equation. Therefore, the abovementioned optimization method can more accurately obtain the waveform energy compared with the traditional numerical discrete integration and integration based on the Gaussian kernel formula.

C. Model Verification

The validation of the algorithm framework primarily focuses on the validation of model parameter d. If the model parameters are accurately obtained, then the accuracy of XCO$_2$ will also be greatly improved. In the parameter group of the model, model parameter d reflects the length of the CO$_2$ cylinder, and it is verifiable. Therefore, the validation of model parameter d can reflect the accuracy of the algorithm framework and the model's inversion of XCO$_2$.

The model validation was divided into sea and land based on the different surface types. First, we validated the tidal data from the Qinhuangdao site on the sea surface. Second, we validated the ICESat-2 data in plain and mountainous areas. We need to reevaluate the offset of latitude and longitude to obtain accurate surface elevation values of the lidar footprints. Then, we match the ICESat-2 data as the surface elevation based on the offset lidar footprint coordinates of point D in Fig. 3. Fig. 3 shows the effect of airborne attitude angle, which causes the true lidar footprint to deviate from the sub-aircraft point. Specifically, the location of the sub-aircraft point (the GPS value) does not represent the true location of the footprint.

Assuming that the attitude angle of the aircraft does not change, the sub-aircraft point path observed by the 1.572-μm IPDA lidar is OA. However, the path observed by the 1.572-μm IPDA lidar in the experiment is OD due to the combined influence of the roll and pitch angles. Specifically, AD is the deviation distance (approximately 330 m) of the actual footprint and the sub-aircraft point. Therefore, the true location of the LiDAR footprints must be reevaluated because the GPS data do not represent the true location of lidar footprints. We use the following formula to obtain the deviation from latitude and longitude:

$$L_{\mathrm{AD}} = L_{\mathrm{OD}} \sin\left(\mathrm{arcos}(\cos(\mathrm{Pa})\cos(\mathrm{Ra}))\right) \tag{6}$$

$$L_{\mathrm{AC}} = L_{\mathrm{OD}} \cos\left(\mathrm{arcos}(\cos(\mathrm{Pa})\cos(\mathrm{Ra}))\right) \tan(\mathrm{Pa}) \tag{7}$$

$$L_{CD} = L_{\mathrm{OD}} \sin(\mathrm{Ra}) \tag{8}$$

$$\alpha = \mathrm{atan}(V_N/V_E) \tag{9}$$

$$\beta = (L_{\mathrm{AC}}^2 + L_{\mathrm{AD}}^2 - L_{CD}^2)/(2L_{\mathrm{AC}}L_{\mathrm{AD}}) \tag{10}$$

$$\Delta_{\mathrm{Lat}} = L_{\mathrm{AD}}\sin(\Delta_{\alpha\beta})/111321 \tag{11}$$

$$\Delta_{\mathrm{Lon}} = L_{\mathrm{AD}}\cos(\Delta_{\alpha\beta})/(\cos(\mathrm{Lat})111321) \tag{12}$$

where L_{OD} is the range [the OD in Fig. 3(a)] detected by lidar from the above theory; Pa is the pitch angle; Ra is the roll angle; V_N is the northbound speed; V_E is the east speed; and L_{AD}, L_{AC}, and L_{CD} represent model distances from AD, AC, and CD in Fig. 3(a), respectively. Variable α represents the deviation angle of the aircraft between the actual flight direction and east. Fig. 3(c) shows β in detail in the plane formed by points A, C, and D. $\Delta_{\alpha\beta}$ represents the difference between α and β. Δ_{Lat} and Δ_{Lon} represent the offset from point D relative to point A, respectively.

IV. EXPERIMENTAL RESULTS

A. Experimental Results Based on the Abovementioned Model Functions

We performed the same processing for each set of signals based on the algorithmic framework mentioned above to extract the valid signals from the raw data. In this process, we build model equations and obtain the model parameters by combining each echo component to fit in the signal. Fig. 4 shows the processing results of the multiple subcomponents in a single signal.

We obtained the model parameters of the subcomponents in the raw signal data through model fitting and LM algorithm optimization in the algorithm framework, as shown in Fig. 4(a). Then, we remove the optimized model energy [the red curve in Fig. 4(a)] from the original energy data. This remaining energy is called the difference data [the gray dot in Fig. 4(b)]. Subsequently, we started the model parameter fitting and optimization of the signal subcomponent in Fig. 4(b) based on the difference data and obtained the corresponding model parameters. We completed the quantization of the signal components and demonstrated the quantized model through the superposition of multiple subsignals in Fig. 4(c).

Fig. 4(d) shows the remaining energy distribution, which is called Gaussian white noise, when the energy of the superimposed subcomponents of the model is removed from the original data. In particular, we performed statistics in the form of a histogram in Fig. 4(d). The results showed a nearly normal distribution, as shown in Fig. 4(e), which was consistent with the distribution characteristics of Gaussian white noise. The abovementioned results show that the signal data are well quantified by our algorithm model.

The 1.572-μm IPDA lidar signal was divided into four types (sea surface, plain, mountain, and cloud) in the study area. We selected the coefficient of determination (R^2), which was used to quantitatively evaluate the relationship between the quantized signal energy and the original data energy. The
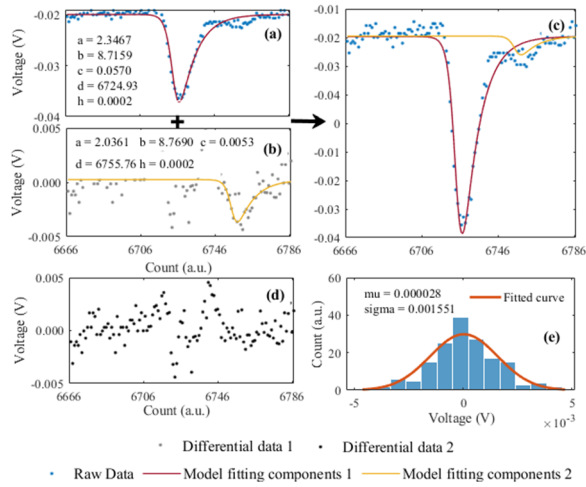
Fig. 4. Model processing results. The processing results of each step for the received λ_{OFF} signal are mainly shown in this figure, and the lidar footprint is located on the sea surface. (a) Results of first model component fitting. (b) Results of second model component fitting. (c) Results of first and second model component fits based on the original data. (d) Residuals after the effective signal has been extracted. (e) Statistical results of the residuals in Fig. 4(d).

Fig. 5. Raw signal data from bands λ_{ON} and λ_{OFF} for the multiple signal types.

visualization results of the quantitative description of the signal are shown in Fig. 5. The results demonstrate that the model has high robustness for the different signal types, and its evaluation index R^2 is almost higher than 0.97 for the four types of lidar signals. In particular, the model can be well quantified for cloud and ground signals that may cause multiple echoes. The model function can better quantify the 1.572-μm IPDA lidar signal.

B. Model Validation

To further verify the algorithm framework, we divide the validation into sea and land based on the validation idea and specific experimental conditions. We compare the GPS value provided by the aircraft with the difference between the vertical CO_2 column length from the aircraft platform to the sea surface and the sea surface height in the WGS84 coordinate system to verify the sea surface. The real-time sea surface height mainly consists of two components: the elevation of the tide survey station (Qinhuangdao station) and the real-time tide data [data in Fig. 6(a)]. In addition, the data of the tide survey station involved the conversion from the 1985 elevation system data to the WGS84 elevation system data, and the conversion value ξ [Fig. 6(b)] was obtained through the EGM2008 gravity model calculation.

In Fig. 6(c), we compare the value of the GPS height with the value after the deviation was corrected (the value is the sum of the two values, the corrected vertical CO_2 column length, and the real-time sea surface height). The results show that the accuracy of our algorithm framework on the sea surface is 0.74 m relative to the measured height of about 6800 m. In addition, the Pearson coefficient is 1.00, demonstrating the presence of a significant correlation between the data at the 0.01 level, which further indicates that the accuracy of our algorithm framework has high robustness in sea surface.

We compared the difference between the GPS data and the deviation correction value in Fig. 7(a) to verify the effect of the model on land. The deviation correction value mainly
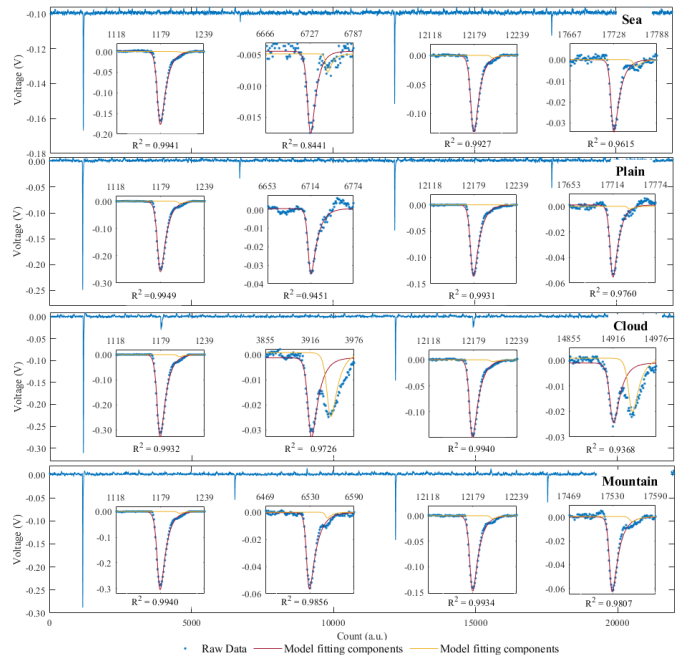
includes two items, namely, the vertical CO_2 column distance [the algorithm results in Fig. 7(a)] and the surface elevation value of the corresponding lidar footprint. The mean of the height error of the ICESat-2_ATL08 terrain is less than 0.05 m in the plain region and 0.5 m in the mountain region [25]. Considering that the IPDA lidar and ICESat-2_ATL08 data are in the WGS84 coordinate system, we use the ICESat-2_ATL08 data as the surface elevation input data. Meanwhile, we matched the 1.572-μm IPDA lidar data with the ICESat-2_ATL08 data and labeled the matched 1.572-μm IPDA lidar data as plains or mountains in Fig. 7.

We show the results of the algorithm model validation on land, with an accuracy of 6.20 m, in Fig. 7(b). The low accuracy of this algorithm framework on land is mainly due to the validation dataset. The ICESat-2_ATL08 data were collected from December 2018 to December 2021 to increase the number of high-precision validation data. Moreover, we used a rectangular box range of 8 m to match the footprint data of ICESat-2 and 1.572-μm IPDA lidar. This work also introduces some errors when the local terrain is complex. In addition, a certain error in the validation data was observed compared with the 1.572-μm IPDA lidar data collected in March 2019. Therefore, the validation on the sea surface is more representative of the model validation.

In this section, we use parameter d to verify the accuracy rates of the algorithm framework in the study area, which are 0.74 and 6.20 m in the sea and land, respectively. The accuracy of land is low compared with that of sea because of the uncertainty error in the land verification dataset. Therefore, the verification of the algorithm framework on the water can better reflect the accuracy. Overall, the algorithm framework has better accuracy and robustness.

C. XCO₂ Optimization by the Model

We show three different IWFs (optimized IWF (OIWF), FIWF, and NIWF) for optimization in Fig. 8(a). The OIWF is
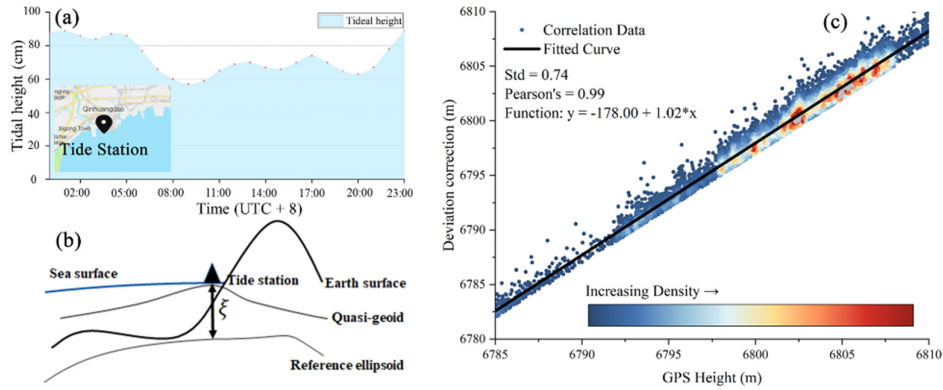
Fig. 6. Algorithm validation results on the sea surface. (a) Geographical location and tidal height data of the tide survey station. (b) Elevation anomalies between the 1985 elevation system and the WGS84 elevation system were visualized. (c) Statistical results.
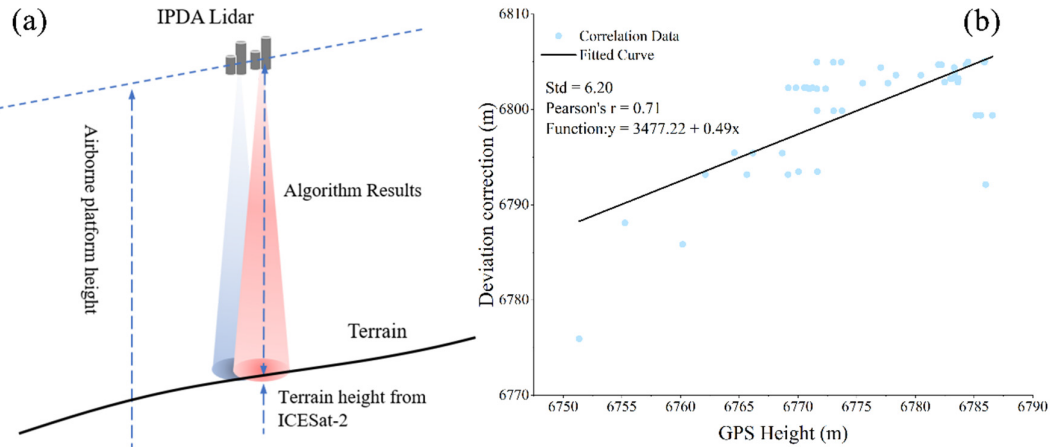

Fig. 7. Algorithm validation results on the land surface. (a) Validation model of the algorithm on the land surface type. (b) Statistical results.
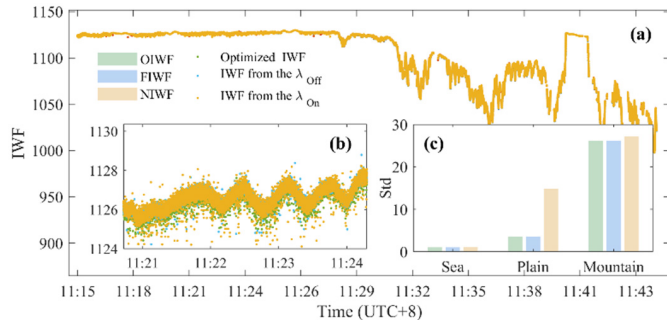

Fig. 8. Visualization of the results of the OIWF. OIWF is the optimized IWF. FIWF is obtained from λ_{OFF}, and NIWF is obtained from λ_{ON}. (a) Three different IWF (OIWF, FIWF, and NIWF). (b) Zooms in on the local information of Fig. 8(a). (c) Standard deviation results for the three IWF in three different surface types (sea, plain, and mountain).
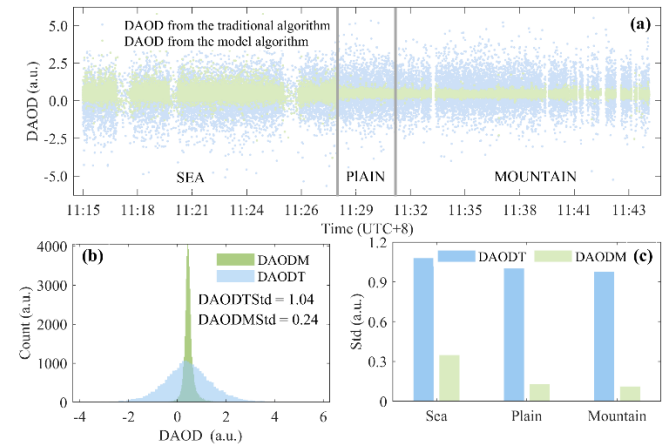

Fig. 9. Visualization of the results of the optimized DAOD. DAODM is the optimized DAOD based on the model. DAODT is obtained from the traditional algorithm. (a) Results of DAODT and DAODM. (b) Statistical results of Fig. 9(a). (c) Standard deviation results of the DAODT and DAODM in three different surface types (sea, plain, and mountain).

the optimized IWF based on the direct adjustment theory of unequal precision. The FIWF is the calculated IWF through λ_{OFF}. The NIWF is the calculated IWF through λ_{ON}. We have enlarged the local information of Fig. 8(a) in Fig. 8(b) because the differences between OIWF, FIWF, and NIWF are relatively small. Furthermore, we counted the standard deviations of the three IWFs in three different surface types (sea, plain, and mountain) in Fig. 8(c).

The standard deviation was adopted as the evaluation index, and the smaller standard deviation indicated better results. For ocean and plain areas, the standard deviation of OIWF is close to that of FIWF, but the standard deviation of OIWF is lower than that of NIWF, as shown in Fig. 8(c). However,

in mountainous areas, the standard deviation of OIWF is lower than those of FIWF and NIWF. Therefore, compared to FIWF and NIWF, the OIWF from our model has a good advantage, especially in mountainous areas.

We compare the traditional energy integration and the proposed theory in Fig. 9(a) to optimize the DAOD. The DAODM is the optimized DAOD from the proposed model in this article. The DAODT is the DAOD that is calculated from the traditional discrete energy integral. Fig. 9(b) shows
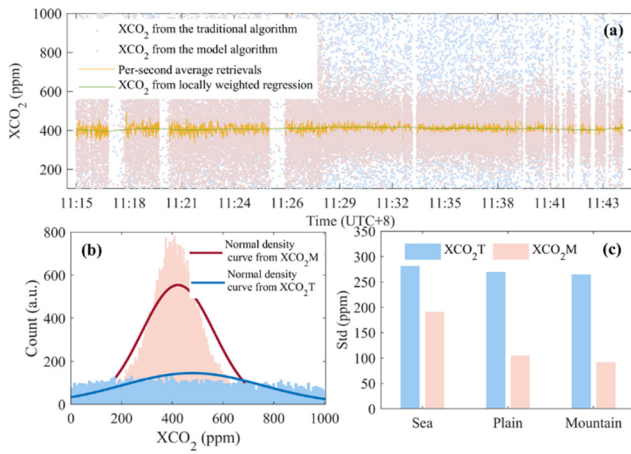
Fig. 10. Visualization of the results of the optimized XCO_2. (a) Results of XCO_2T and XCO_2M. (b) Statistical results of Fig. 10(a). (c) Standard deviation results of XCO_2T and XCO_2M in three different surface types (sea, plain, and mountain).

Fig. 11. XCO_2 validation. The 1.572-μm IPDA lidar data in the plain area are marked with rectangular boxes in Fig. 11.

the statistical results of Fig. 9(a), which demonstrates that DAODM is more aggregated relative to DAODT. This finding is also consistent with the actual situation. The DAOD of the airborne data does not drastically change because XCO_2 does not significantly fluctuate over a distance in the horizontal direction. In addition, we use the standard deviation as an evaluation metric, and the accuracy of the model optimization is improved by 77% compared with the traditional algorithm. The standard deviations of DAODT and DAODM are 1.04 and 0.24, respectively. Furthermore, we show the distribution of the standard deviation over three different surface types (sea, plain, and mountain), and the model improves the accuracy by 67%, 86%, and 88% for the sea, plains, and mountains, respectively.

We compare the traditional algorithm with the optimized algorithm in Fig. 10(a) to optimize XCO_2. The XCO_2M is XCO_2 based on the theory proposed in this work in Fig. 10(a). The XCO_2T is XCO_2 based on the traditional algorithm. Fig. 10(b) shows the statistical results from Fig. 10(a), and the density curve of XCO_2 presents a normal distribution. In Fig. 10(b), the XCO_2M data distribution is more aggregated than XCO_2T. In particular, we have calculated the standard deviation of XCO_2 in three surface types (sea surface, plain, and mountain) in Fig. 10(c). The results show that XCO_2M increases by 31%, 63%, and 66% relative to XCO_2T. The yellow line represents the average XCO_2M per second in Fig. 10(a). The mean values of XCO_2 at the sea level, plain, and mountain are 409.91, 416.14, and 411.83 ppm, with standard deviations of 9.60, 8.34, and 7.77 ppm, respectively.

D. Accuracy Verification With OCO-2

We perform an indirect comparison with the OCO-2 satellite data in Figs. 11 and 12 for the accuracy assessment of the optimized XCO_2. We discovered that the OCO-2 satellite data are available on March 14 and March 16 because the OCO-2 data are close to the airborne experimental data in time and space.

The experimental data were classified as ocean, plains, and mountains according to the type of surface, as shown in Fig. 11. The mean values of XCO_2 for the airborne experi-
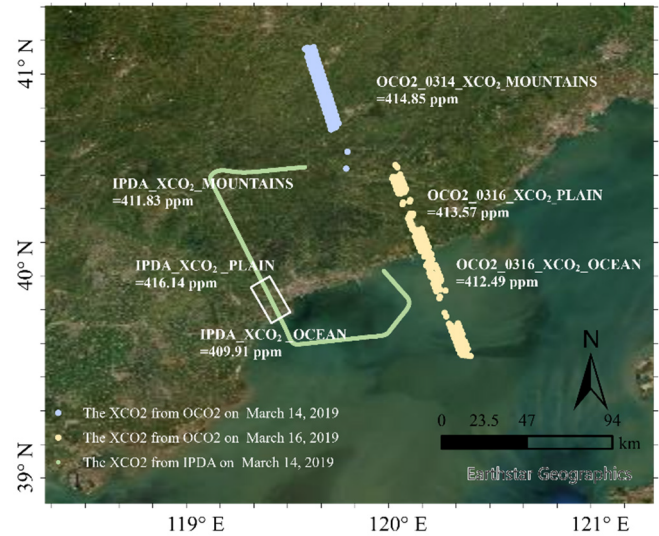
ments were 409.91, 416.14, and 411.83 ppm. The OCO-2 data were classified as ocean, plain, and mountainous according to their location in space, and the mean XCO_2 values were calculated to be 412.49, 413.57, and 414.85 ppm for the corresponding regions. By contrast, this XCO_2 from IPDA lidar has changed by −2.58, 2.57, and −3.02 ppm in ocean, plain, and mountain relative to the OCO-2 data, respectively. The difference XCO_2 for the two different platforms is mainly due to the detection mechanisms between the OCO-2 satellite and the IPDA lidar. Specifically, the XCO_2 from the OCO-2 satellite is the full atmospheric column concentration. Meanwhile, the XCO_2 from IPDA lidar is the atmospheric column concentration from the surface to the aircraft. We also discovered that the measured XCO_2 in the mountains is about 2 ppm higher than that in the ocean for both platforms, indicating that the XCO_2 changes from the OCO-2 satellite and the IPDA lidar are consistent.

We performed tests for the XCO_2 trendiness from the OCO-2 satellite and IPDA lidar in Fig. 12. The averaged XCO_2 of the IPDA lidar is calculated at fixed latitudinal intervals (0.01°) based on the trajectory of the airborne flight. We also calculated the mean of XCO_2 for each latitude interval (0.01°) based on the OCO-2 data on March 16. Fig. 12 shows the mean XCO_2 changes at different latitudes based on two observation platforms.

The XCO_2 monitoring by the OCO-2 passive satellite is considered relatively reliable. Accordingly, we chose the OCO-2 data as a reference for the trend analysis. The XCO_2 changes of the IPDA lidar and OCO-2 have basically the same trend in Fig. 12. In particular, the trend is clearly consistent, as shown in the shaded rectangular box in Fig. 12(a)–(c). The reason for the inconsistent trend in the middle part of Fig. 12 lies in the different observation times of the platforms and the type of surface. In terms of observation time, IPDA lidar was observed on March 14 at 11:00 local time. OCO-2 satellite was observed on March 16 at 13:00 local time. Furthermore, the area detected by IPDA lidar for the type of surface observations is urban with high anthropogenic activity factors at 39.80 and 39.97 N. However, the corresponding areas
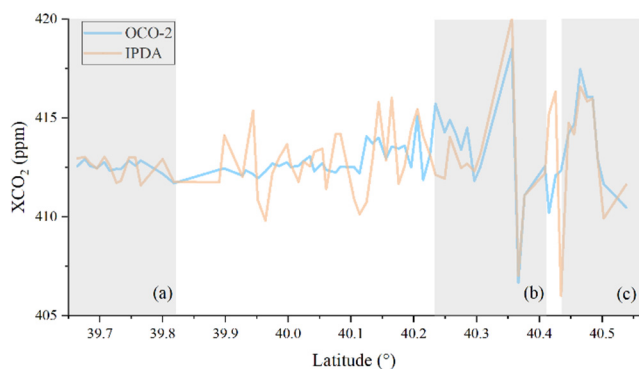
Fig. 12. Trend validation results.

detected by the OCO-2 satellite are rural and cultivated fields with relatively weak anthropogenic activity factors. Overall, our algorithm is highly accurate and consistent.

V. CONCLUSION AND DISCUSSION

The existing XCO_2 inversion assumes that the signal is idealized Gaussian based on the IPDA lidar. In addition, the calculation of IWF and DAOD is separated in the traditional theory of calculation. Specifically, the required parameters are not from the same equation for computing IWF and DAOD. Therefore, a theory is needed to optimize the error caused by parameter transfer. In this work, we propose a model based on spectral energy, which can well match the experimental non-Gaussian signal waveform, especially for the multiwavelet from mountains or clouds. Moreover, we can obtain multiple parameters to calculate IWF and DAOD based on the above core equations, thus effectively improving the accuracy of the algorithm.

During the model validation, the 1.572-μm IPDA lidar column length (from the parameter d conversion) is used indirectly to evaluate the accuracy of the spectral energy model for signal extraction. The experimental results show that the accuracy of the 1.572-μm IPDA lidar column length is 0.74 and 6.20 m at sea and on land based on the indirect evaluation of the length of the 1.572-μm IPDA lidar column length, respectively. The validation sets have errors on land because of the large time interval of the validation data collected on land. The model verification on the sea surface reflects the accuracy of our algorithm. In addition, the sea surface model verification accuracy indicates that the algorithm accuracy has entered the subunit compared with an IPDA lidar spatial resolution of 1.2 m. Furthermore, we verify the optimization of IWF, DAOD, and XCO_2. The IWF optimized by the model was superior to the IWF calculated by λ_{ON} or λ_{OFF}. In particular, the optimization effect of our model is more prominent in the mountainous areas. Our overall DAOD performance improved by about 77% compared with those of the traditional algorithms, especially in the sea, plain, and mountain areas, by 67%, 86%, and 88%, respectively. Finally, the optimized XCO_2 was less scattered (standard deviation as an evaluation metric) and its accuracy was reduced by 31%, 63%, and 66% in the ocean, plains, and mountains, respectively, compared with the traditional algorithm. In addition, we evaluated the mean XCO_2 values of 409.91, 416.14, and 411.83 ppm for the sea, plains, and mountains based on the 1-s interval of the averaged XCO_2, respectively. Our algorithm calculates the XCO_2 with high accuracy and consistency with XCO_2 from the OCO-2 satellite as a reference. In particular, the XCO_2 is more accurate in areas dominated by anthropogenic factors, due to the accuracy of the IPDA detection mechanism.

High-precision active CO_2 monitoring is becoming increasingly important with the deepening research on carbon cycle and neutralization. The airborne experimental data were collected based on a spaceborne scale model in Qinhuangdao, China. Based on this airborne experiment, we designed an algorithm for detecting XCO_2 using the 1.572-μm IPDA lidar. This algorithm improves the accuracy and robustness of the XCO_2 inversion and has important reference significance for the IPDA lidar carried by China's satellites to be launched in the coming years. In the future, we will carry out related work and try to integrate XCO_2 data based on active IPDA lidar and passive observation satellite products.

REFERENCES

[1] J.-R. Petit and D. Raynaud, "Forty years of ice-core records of CO_2," *Nature*, vol. 579, no. 7800, pp. 505–506, Mar. 2020.

[2] *Carbon Dioxide Levels Continue at Record Levels, Despite COVID-19 Lockdown*. Accessed: Dec. 8, 2022. [Online]. Available: https://public.wmo.int/en/media/press-release/carbon-dioxide-levels-continue-record-levels-despite-covid-19-lockdown

[3] *China's Carbon Peaking and Carbon Neutral Policies*. Accessed: Dec. 8, 2022. [Online]. Available: http://www.gov.cn/xinwen/2021-04/02/content_5597403.htm

[4] T. Shi et al., "Measurement of CO_2 rectifier effect during summer and winter using ground-based differential absorption LiDAR," *Atmos. Environ.*, vol. 220, pp. 117097–117107, Jan. 2020.

[5] T. Shi et al., "An inversion method for estimating strong point carbon dioxide emissions using a differential absorption LiDAR," *J. Clean. Prod.*, vol. 271, pp. 122434–122446, Oct. 2020.

[6] A. Amediek, X. Sun, and J. B. Abshire, "Analysis of range measurements from a pulsed airborne CO_2 integrated path differential absorption LiDAR," *IEEE Trans. Geosci. Remote Sens.*, vol. 51, no. 5, pp. 2498–2504, May 2013.

[7] X. Ma et al., "On-line wavenumber optimization for a ground-based CH_4-DIAL," *J. Quant. Spectrosc. Radiat. Transf.*, vol. 229, pp. 106–119, May 2019.

[8] X. Ma et al., "High-precision CO_2 column length analysis on the basis of a 1.57-μm dual-wavelength IPDA LiDAR," *Sensors*, vol. 20, no. 20, p. 5887, Oct. 2020.

[9] Y. Gong, L. Bu, B. Yang, and F. Mustafa, "High repetition rate mid-infrared differential absorption LiDAR for atmospheric pollution detection," *Sensors*, vol. 20, no. 8, p. 2211, Apr. 2020.

[10] Y. Zhu, J. Liu, X. Chen, X. Zhu, D. Bi, and W. Chen, "Sensitivity analysis and correction algorithms for atmospheric CO_2 measurements with 1.57m airborne double-pulse IPDA LIDAR," *Opt. Exp.*, vol. 27, pp. 32679–32699, Oct. 2019.

[11] K. L. Chan et al., "Evaluation of ECMWF-IFS (version 41R1) operational model forecasts of aerosol transport by using ceilometer network measurements," *Geosci. Model Develop.*, vol. 11, no. 9, pp. 3807–3831, Sep. 2018.

[12] S. Houweling et al., "Evidence of systematic errors in SCIAMACHY-observed CO_2 due to aerosols," *Atmos. Chem. Phys.*, vol. 5, pp. 3003–3013, Nov. 2005.

[13] M. Buchwitz et al., "Atmospheric methane and carbon dioxide from SCIAMACHY satellite data: Initial comparison with chemistry and transport models," *Atmos. Chem. Phys.*, vol. 5, no. 4, pp. 941–962, Mar. 2005.

[14] I. Aben, O. Hasekamp, and W. Hartmann, "Uncertainties in the space-based measurements of CO$_2$ columns due to scattering in the Earth's atmosphere," *J. Quant. Spectrosc. Radiat. Transf.*, vol. 104, no. 3, pp. 450–459, Apr. 2007.

[15] X. Ma et al., "Regional atmospheric aerosol pollution detection based on LiDAR remote sensing," *Remote Sens.*, vol. 11, pp. 2339–2358, Oct. 2019.

[16] A. K. Ramanathan et al., "A singular value decomposition framework for retrievals with vertical distribution information from greenhouse gas column absorption spectroscopy measurements," *Atmos. Meas. Techn.*, vol. 11, no. 8, pp. 4909–4928, Aug. 2018.

[17] B. Liu et al., "The relationship between atmospheric boundary layer and temperature inversion layer and their aerosol capture capabilities," *Atmos. Res.*, vol. 271, Jun. 2022, Art. no. 106121.

[18] T. Shi et al., "Retrieving CH4-emission rates from coal mine ventilation shafts using UAV-based aircore observations and the genetic algorithm–interior point penalty function (GA-IPPF) model," *Atmos. Chem. Phys.*, vol. 22, no. 20, pp. 13881–13896, Oct. 2022.

[19] T. Shi et al., "Quantifying CO$_2$ uptakes over oceans using LIDAR: A tentative experiment in Bohai Bay," *Geophys. Res. Lett.*, vol. 48, no. 9, May 2021, Art. no. e2020GL091160.

[20] J. Abshire et al., "Airborne measurements of CO$_2$ column concentration and range using a pulsed direct-detection IPDA LiDAR," *Remote Sens.*, vol. 6, no. 1, pp. 443–469, Dec. 2013.

[21] T. F. Refaat, U. N. Singh, J. Yu, M. Petros, R. Remus, and S. Ismail, "Airborne two-micron double-pulse IPDA lidar validation for carbon dioxide measurements over land," *EPJ Web Conf.*, vol. 176, p. 5001, Apr. 2018.

[22] U. N. Singh et al., "Feasibility study of a space-based high pulse energy 2μm CO$_2$ IPDA LiDAR," *Appl Opt.*, vol. 56, pp. 6531–6547, Apr. 2018.

[23] Y. Zhu, J. Liu, X. Chen, X. Zhu, D. Bi, and W. Chen, "Sensitivity analysis and correction algorithms for atmospheric CO$_2$ measurements with 1.57-μm airborne double-pulse IPDA LiDAR," *Opt. Exp.*, vol. 27, pp. 32679–32699, Oct. 2019.

[24] C. Xiang et al., "Design of inversion procedure for the airborne CO$_2$-IPDA LIDAR: A preliminary study," *IEEE J. Sel. Topics Appl. Earth Observ. Remote Sens.*, vol. 14, pp. 11840–11852, Nov. 2021.

[25] X. Tian and J. Shan, "Comprehensive evaluation of the ICESat-2 ATL08 terrain product," *IEEE Trans. Geosci. Remote Sens.*, vol. 59, no. 10, pp. 8195–8209, Oct. 2021.

[26] G. Ehret, C. Kiemle, M. Wirth, A. Amediek, A. Fix, and S. Houweling, "Space-borne remote sensing of CO$_2$, CH$_4$, and N$_2$O by integrated path differential absorption LiDAR: A sensitivity analysis," *Appl. Phys. B, Lasers Opt.*, vol. 90, nos. 3–4, pp. 593–608, Jan. 2008.

Haowei Zhang received the B.S. degree in remote sensing science and technology from the Heilongjiang Institute of Engineering, Harbin, China, in 2019, and received the M.S. degree from Wuhan University, Wuhan, China, in 2022. He is currently pursuing the Ph.D. degree with Wuhan University, Wuhan, China.

His research interests include lidar ranging and remote sensing of environment.

Ge Han received the B.S. and M.S. degrees in geodetection and information technology from the China University of Geosciences, Wuhan, China, in 2009 and 2012, respectively, and the Ph.D. degree in remote sensing from the State Key Laboratory of Information Engineering in Surveying, Mapping and Remote Sensing, Wuhan University, Wuhan, in 2015.

He is currently an Assistant Professor with the International School of Software, Wuhan University. His research interests include atmospheric sounding and remote sensing of environment.

Xin Ma received the B.S., M.S., and Ph.D. degrees from Wuhan University, Wuhan, China, in 2010, 2013, and 2016, respectively.

He is currently an Associate Professor with the State Key Laboratory of Information Engineering in Surveying, Mapping and Remote Sensing, Wuhan University. His research interests include Lidar and atmospheric remote sensing.

Siwei Li, photograph and biography not available at the time of publication.

Hao Xu, photograph and biography not available at the time of publication.

Tianqi Shi, photograph and biography not available at the time of publication.

Jianye Yuan, photograph and biography not available at the time of publication.

Wanqin Zhong, photograph and biography not available at the time of publication.

Yanran Peng, photograph and biography not available at the time of publication.

Jingjing Xu, photograph and biography not available at the time of publication.

Wei Gong (Member, IEEE) received the B.S. degree in photonics engineering from the Huazhong University of Science and Technology (HUST), Wuhan, China, in 1993, the M.S. degree in electronics from the Chinese Academy of Science, Lanzhou, China, in 1996, and the Ph.D. degree in physical electronics from HUST in 1999.

He was an Assistant Professor with Hampton University, Hampton, VA, USA, from 2002 to 2004. He is currently a Professor with the School of Electronic Information, Wuhan University, Wuhan. He is involved in teaching and research of new laser, optical technology, and its remote sensing applications. He has made achievements in atmospheric lidar and optical remote sensing. He has authored more than 100 scientific articles, holds 18 patents, and coauthored two books.

Dr. Gong was a recipient of the New Century Excellent Talents in 2007, the Luojia Scholars and the Chutian Scholars in 2010, and the Yangtze River Scholars in 2014.